Understanding simulated AMOC changes in single-forcing historical experiments

Supplementary Material

Domenico Giaquinto[1*], Dario Nicolì[1], Doug M. Smith[2], Doroteaciro Iovino[1], Dargan M. W. Frierson[3], Simona Masina[1], Panos J. Athanasiadis[1]

[1]CMCC Foundation – Euro-Mediterranean Center on Climate Change, Bologna, Italy.
[2]Met Office Hadley Centre, Exeter, UK.
[3]Department of Atmospheric and Climate Science, University of Washington, Seattle, USA.

*Corresponding author(s). E-mail(s): domenico.giaquinto@cmcc.it;
Contributing authors: dario.nicoli@cmcc.it; doug.smith@metoffice.gov.uk;
dorotea.iovino@cmcc.it; dargan@uw.edu; simona.masina@cmcc.it;
panos.athanasiadis@cmcc.it;

Variable	ACCESS-ESM1-5	CanESM5	CMCC-CM2-SR5	GISS-E2-1-G	HadGEM3-GC31-LL	IPSL-CM6A-LR	MIROC6	MPI-ESM1-2-LR	NorESM2-LM
Ocean overturning mass streamfunction *msftmz* or *msftyz* [kg s^{-1}]	10/3/40	50/30/65	10/10/11	38/40/36	5/5/5	10/10/33	0/0/10	30/30/31	23/23/40
Sea-ice mass *simass* [kg m^{-2}]	3/3/40	50/30/65	10/10/11	45/45/46	55/55/55	6/6/33	50/10/50	0/0/45	20/20/40
Mixed layer depth *mlotst* [m]	10/10/39	50/30/65	10/10/11	39/36/40	55/55/55	9/10/33	0/0/0	30/30/50	23/23/43
Ocean salinity *so* [p.p.t.]	10/10/40	50/30/64	10/10/11	44/41/66	55/55/55	10/10/33	50/10/50	30/30/51	20/20/40
Ocean temperature *thetao* [K]	10/10/40	50/30/64	10/10/11	44/41/47	55/55/55	10/10/33	50/10/50	30/30/51	20/20/40
Downward latent surface heat flux *hfls* [W m^{-2}]	10/10/40	50/30/65	10/10/11	45/45/46	55/55/55	10/10/33	50/10/50	30/30/51	20/20/40
Downward sensible surface heat flux *hfss* [W m^{-2}]	10/10/40	50/30/65	10/10/11	45/45/46	55/55/55	10/10/33	50/10/50	30/30/51	20/20/40
Downward longwave radiative surface heat flux *rlds* [W m^{-2}]	10/10/40	50/30/65	10/10/11	45/45/46	0/0/0	10/10/33	50/10/50	0/0/0	20/20/40
Upward longwave radiative surface heat flux *rlus* [W m^{-2}]	10/10/40	50/30/65	10/10/11	45/45/46	0/0/0	10/10/33	50/10/50	0/0/0	20/20/40
Downward shortwave radiative surface heat flux *rsds* [W m^{-2}]	10/10/40	50/30/65	10/10/11	45/45/46	5/5/0	10/10/33	50/10/50	0/0/0	20/20/40
Upward shortwave radiative surface heat flux *rsus* [W m^{-2}]	10/10/0	50/30/65	10/10/0	45/45/46	5/5/0	10/10/33	50/10/50	0/0/0	20/20/40
Radiative net longwave heat flux *rls* [W m^{-2}]	0/0/40	0/0/0	0/0/11	0/0/0	50/50/55	0/0/0	50/10/0	30/30/51	0/0/0
Radiative net shortwave heat flux *rss* [W m^{-2}]	0/0/40	0/0/0	0/0/11	0/0/0	50/50/55	0/0/0	0/0/0	30/30/51	0/0/0
Precipitation *Pr* [mm mon^{-1}]	10/10/40	50/30/65	10/10/11	45/45/46	55/55/55	10/10/33	50/10/50	30/30/51	23/23/44
Near-surface air temperature *TAS* [K]	3/3/40	50/30/65	10/10/11	45/45/46	5/54/5	10/10/33	50/10/50	0/0/0	20/20/40

Table S1 Variables used in this study. The variable name (plain text), the corresponding CMIP6 ID (in italic), and the unit measure (in square brachets) are reported in the leftmost column. All other columns refer to each one of the analysed models analysed. The respective ensemble sizes per variable, model, and experiment are reported in the cells, with the first number corresponding to the hist-GHG experiment, the second to the hist-aer experiment, and the third to the historical experiment.

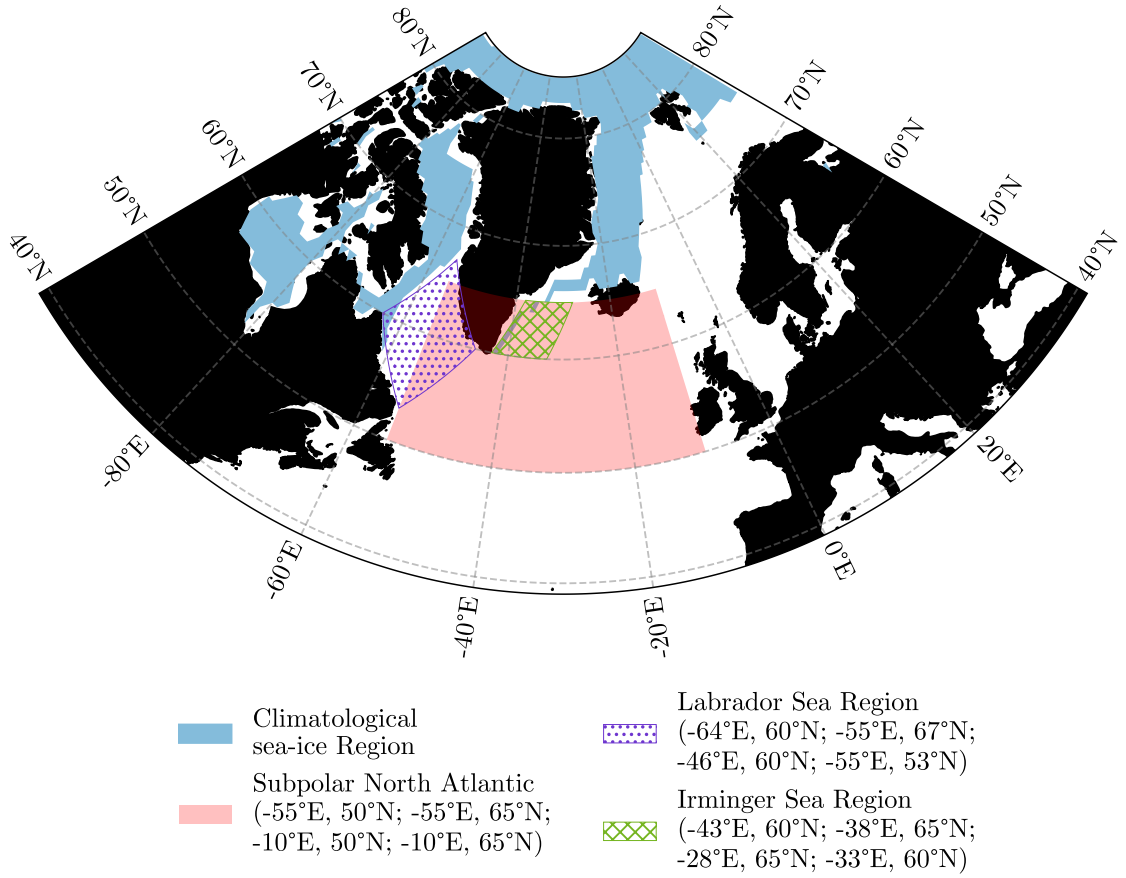


Fig. S1 Spatial regions used in this study. Subpolar North Atlantic (red), Labrador Sea Region (purple dots), and Irminger Sea Region (green hatching). The coordinates of the corners are reported in the legend. The climatological sea-ice Region (light blue) is specific for each experiment, season, and model (see Methods); in this case, the one referring to hist-GHG DJFM NorESM2-LM is shown.

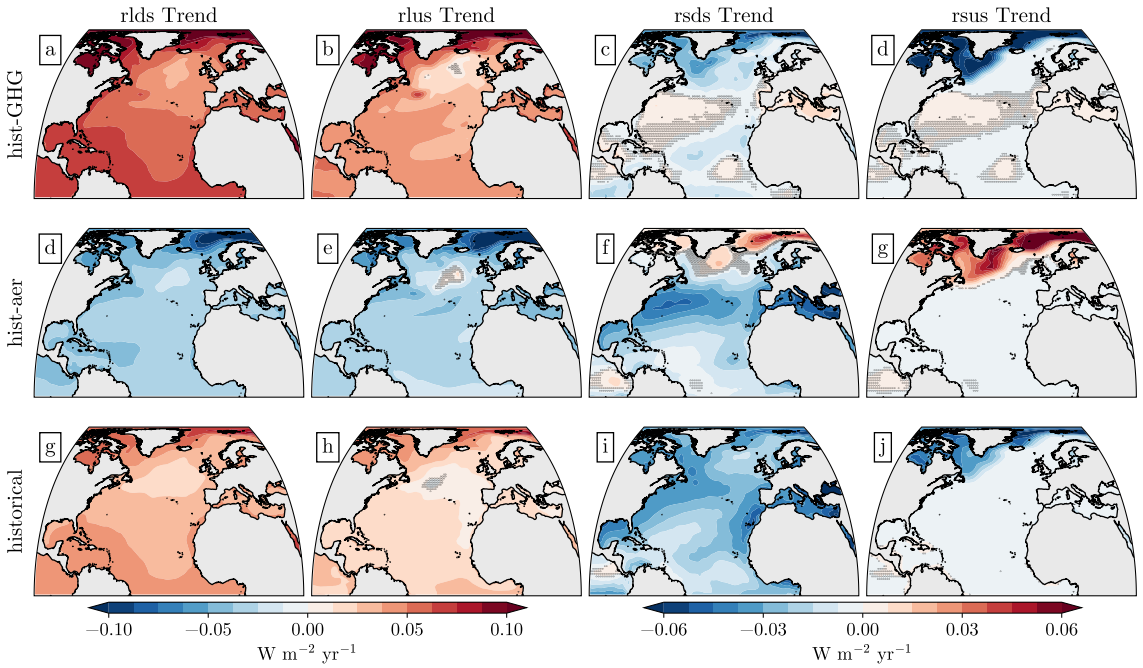


Fig. S2 Trends of the different components of the net radiative surface heat flux. Maps show the multi-model mean linear trends in 1850–2014 of the downward longwave radiative surface heat flux (rlds, first column), the upward longwave radiative surface heat flux (rlus, second column), the downward shortwave radiative surface heat flux (rsds, third column), and the upward shortwave radiative surface heat flux (rsus, fourth column) for the entire year. Hist-GHG experiment (top row), hist-aer experiment (middle row), and historical experiment (bottom row). Stippling indicates regions where the trend is not statistically significant at the 1% level.

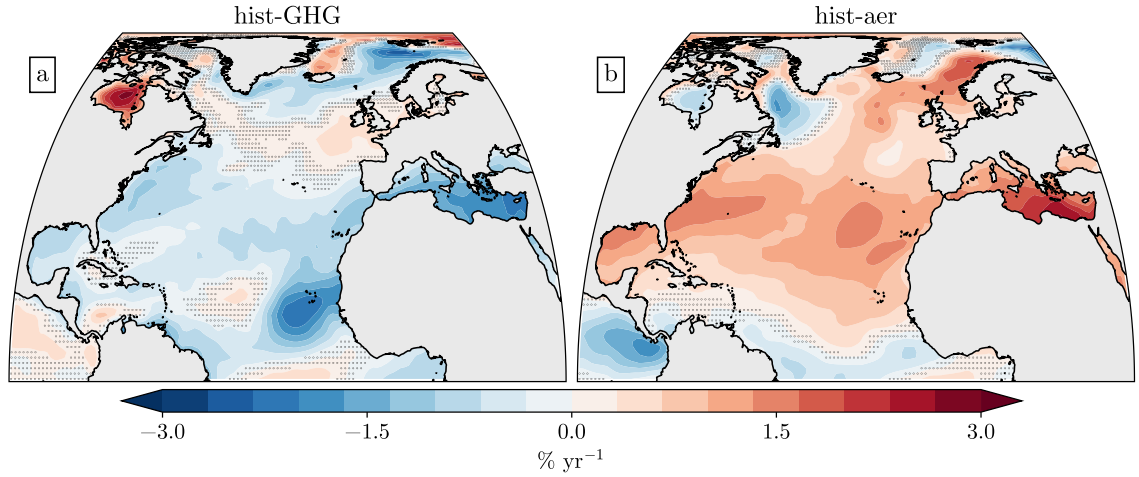


Fig. S3 Trends of clouds fraction. Maps show the multi-model mean linear trends in 1850–2014 of cloud fraction for the **a)** hist-GHG and **b)** hist-aer experiments. Stippling indicates regions where the trend is not statistically significant at the 1% level.

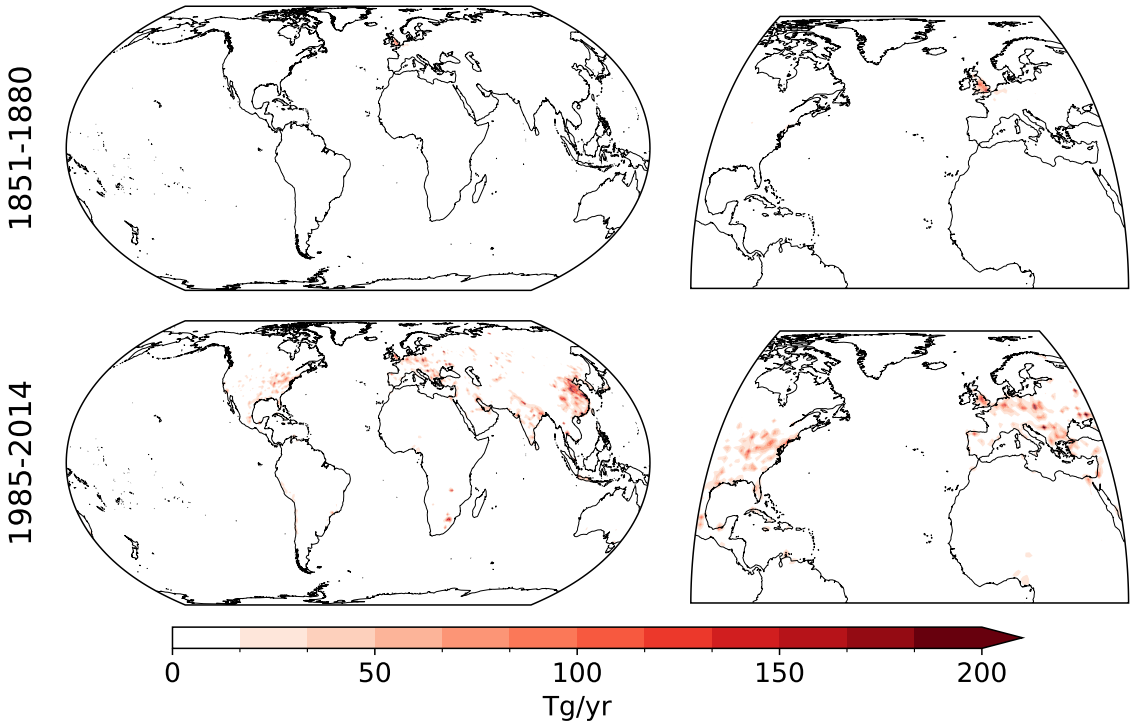


Fig. S4 Spatial distribution of aerosols' emissions as prescribed to the models. Aerosols' emissions in 1851–1880 (top panels) and 1985–2014 (bottom panels) for the entire world (left panels) and for the North Atlantic (right panels). The emissions include black carbon, organic carbon, and sulfur dioxide.

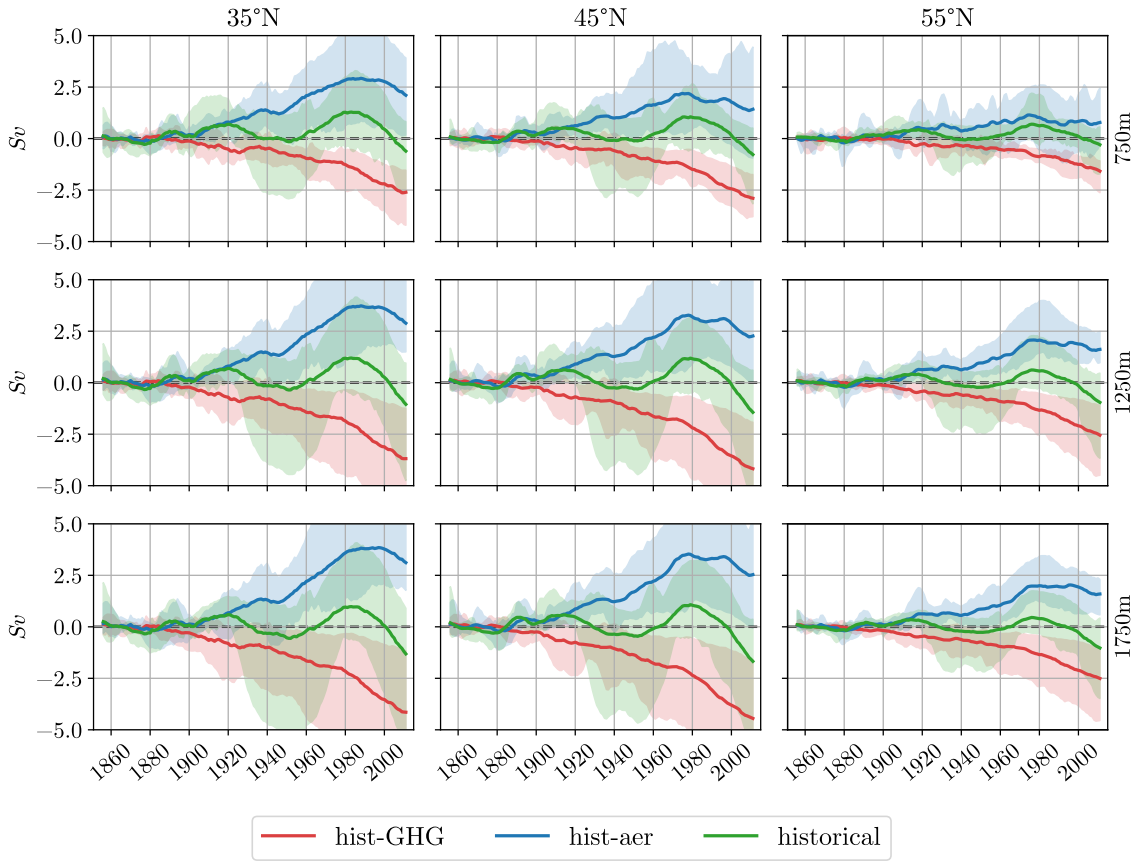


Fig. S5 AMOC strength at different depths and latitudes. Multi-model mean AMOC (solid lines) for the three experiments hist-GHG (red), hist-aer (blue), and historical (green) in 1850–2014. Shades represent the max and min value across the ensemble for the respective experiment. Each column refers to a different latitude, while each row to a different depth. Time series are smoothed with a 10–yr running mean.

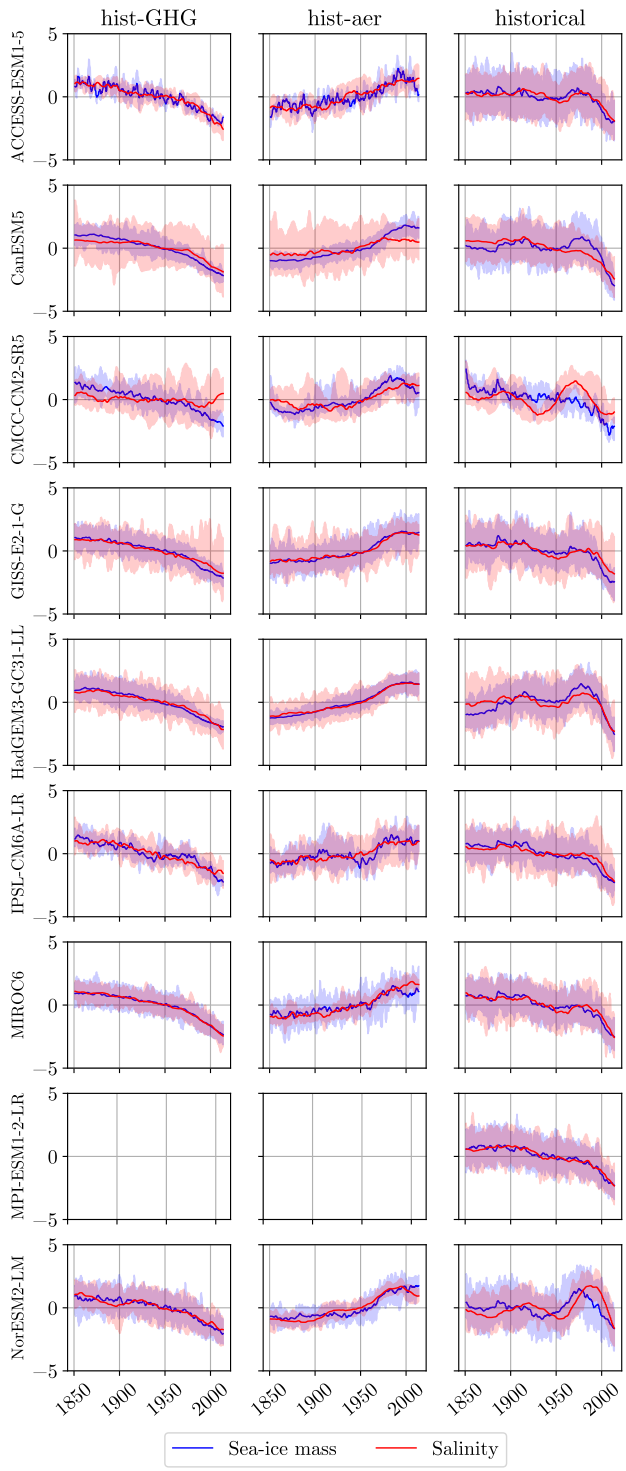


Fig. S6 Sea ice and salinity co-variability. DJFM standardized sea-ice mass and salinity anomalies in 1850—2014 for hist-GHG (left column), hist-aer (middle column), and historical experiments (right column) in the climatological sea-ice region (see Methods). Each row refers to one model (labels on the left). Solid lines represent ensemble-mean sea-ice mass (blue) and salinity (red); shades represent max and min values of the ensemble. Time series are smoothed with a 10–yr running mean. The same behavior is found for all other seasons (not shown).

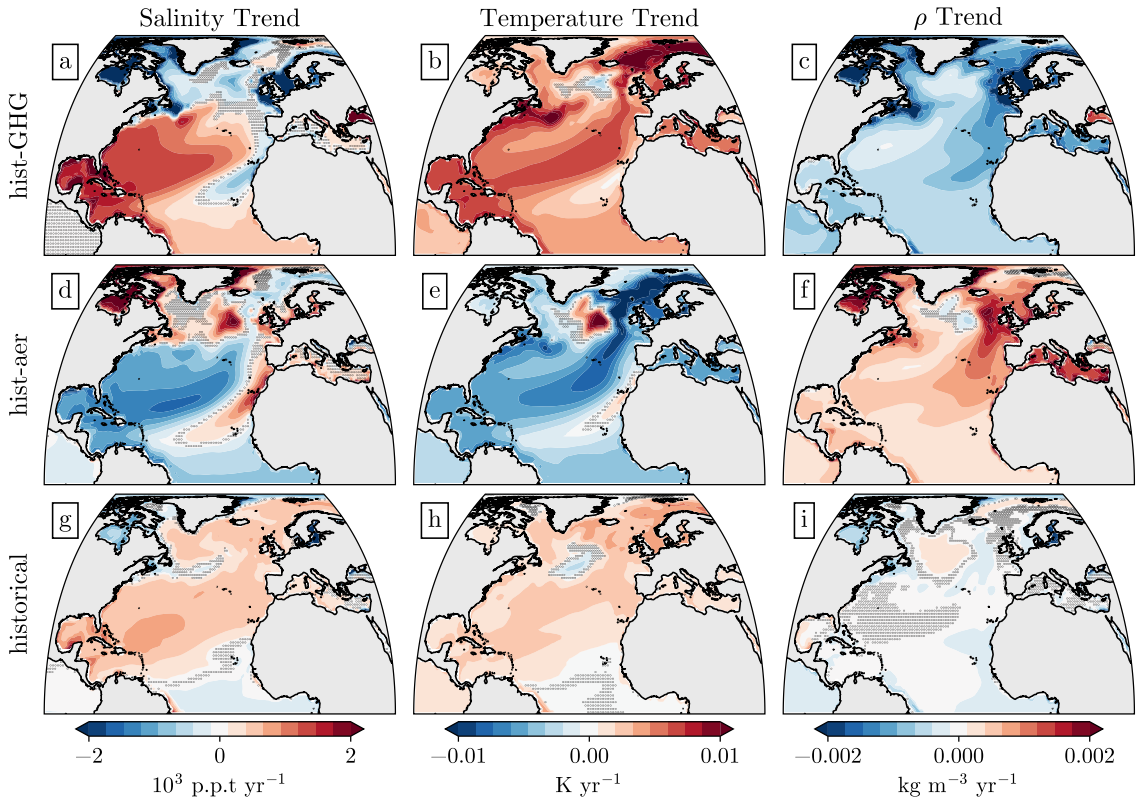


Fig. S7 Upper-ocean (0–500m) Salinity, Temperature, and Density trends. Maps show the DJFM multi-model mean linear trends in 1850–2014 of upper-ocean salinity (left column), upper-ocean temperature (middle column), and upper-ocean density (right column). Hist-GHG experiment (top row), hist-aer experiment (middle row), and historical experiment (bottom row). Stippling indicates regions where the trend is not statistically significant at the 1% level.



Fig. S8 Regression analysis of ρ onto ρ_S and ρ_T. Regression coefficients of ρ onto ρ_S (left column), ρ onto ρ_T (middle column), and difference between the two (right column). Each row refers to one model (labels on the left), with EN4 observations at the last row. Stippling indicates regions where the regression coefficients are not statistically significant. The regressions of the models refer to hist-GHG. The same behavior is found for the other experiments (not shown).

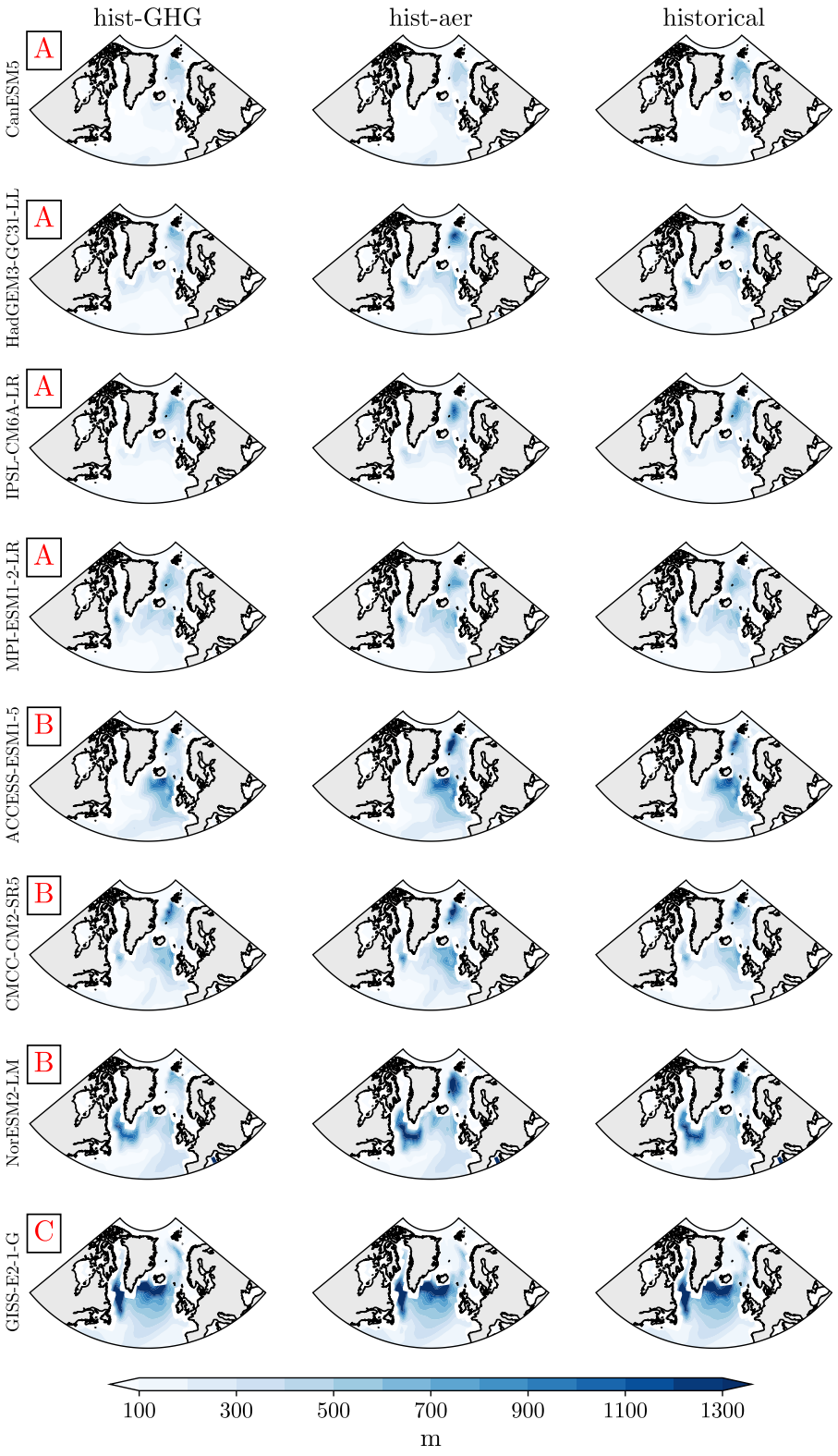


Fig. S9 Mixed layer depth climatology in 1850–2014. Maps show the DJFM ensemble mean 1850–2014 climatology of mixed layer depth for each model and experiment (MIROC6 data were not available). The red capital letters indicate the MLD group to which each model belongs.



Fig. S10 Mixed layer depth trend in 1850–2014. Maps show the DJFM linear trends in 1850–2014 of mixed layer depth for each model and experiment (MIROC6 data were not available). Stippling indicates regions where the trend is not statistically significant at the 1% level.

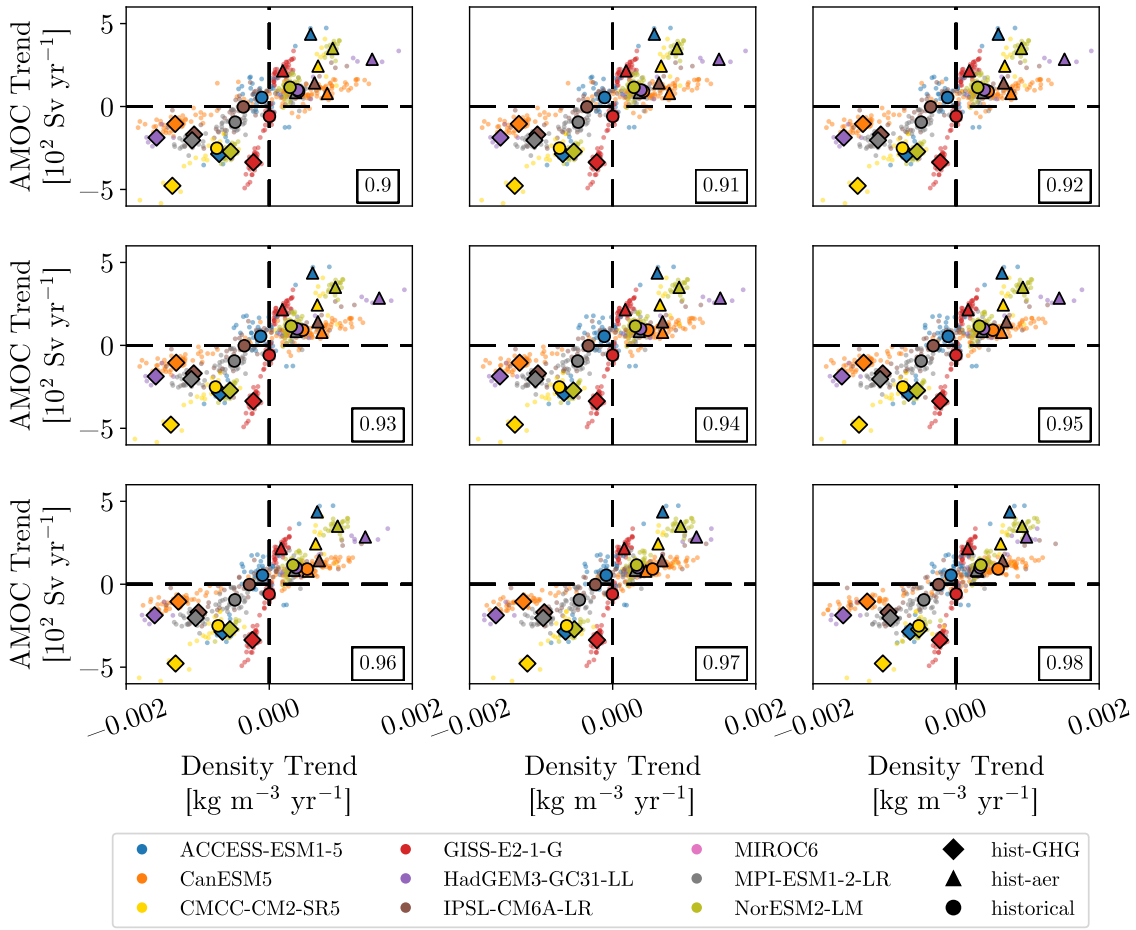


Fig. S11 AMOC and density trends in 1850–2014. Scatter plots of AMOC and density trends during DJFM 1850–2014. Density trends are computed averaging over the respective areas of high climatological MLD. Small dots represent individual members, while markers are ensemble means for each model for hist-GHG (diamonds), hist-aer (triangles), and historical experiments (circles). Each subplot refers to a different threshold used to select the high climatological MLD area (from 0.90 to 0.98, labels on the bottom right of each panel).

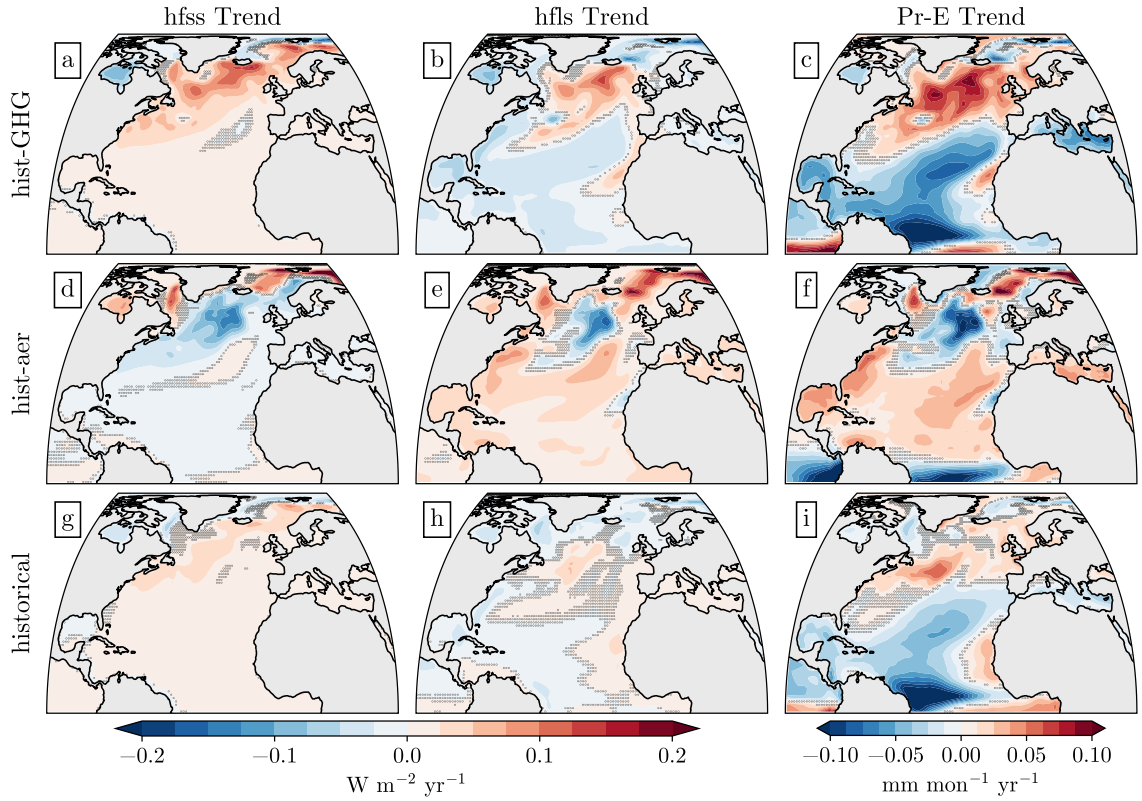


Fig. S12 Trends of surface sensible heat flux, latent heat flux, and freshwater (Pr-E) flux. Maps show the DJFM multi-model mean linear trends in 1850–2014 of sensible heat flux (left column, positive downward), latent heat flux (middle column, positive downward), and Pr-E flux (right column). Hist-GHG experiment (top row), hist-aer experiment (middle row), and historical experiment (bottom row). Stippling indicates regions where the trend is not statistically significant at the 1% level.

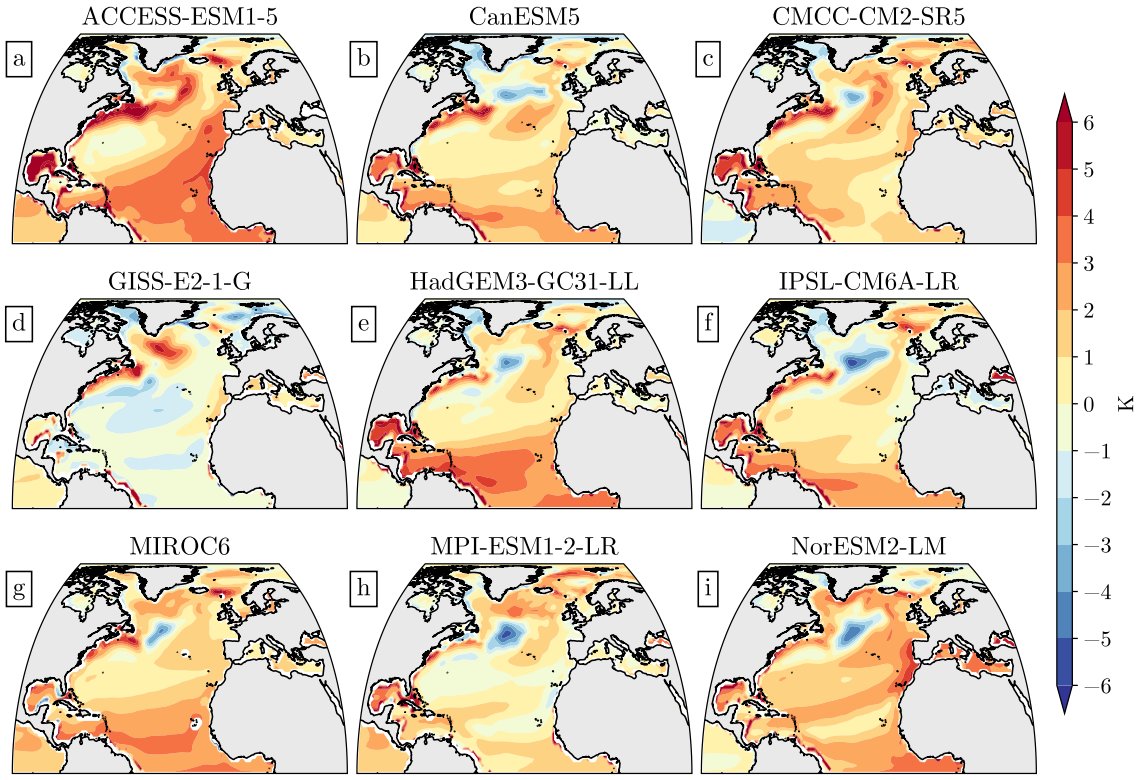


Fig. S13 Comparison between upper-ocean temperature climatology in models and observations. DJFM 1985–2014 upper-ocean temperature climatology difference between each model ensemble mean and the EN4 observations. Results do not change significantly for different time periods (not shown).

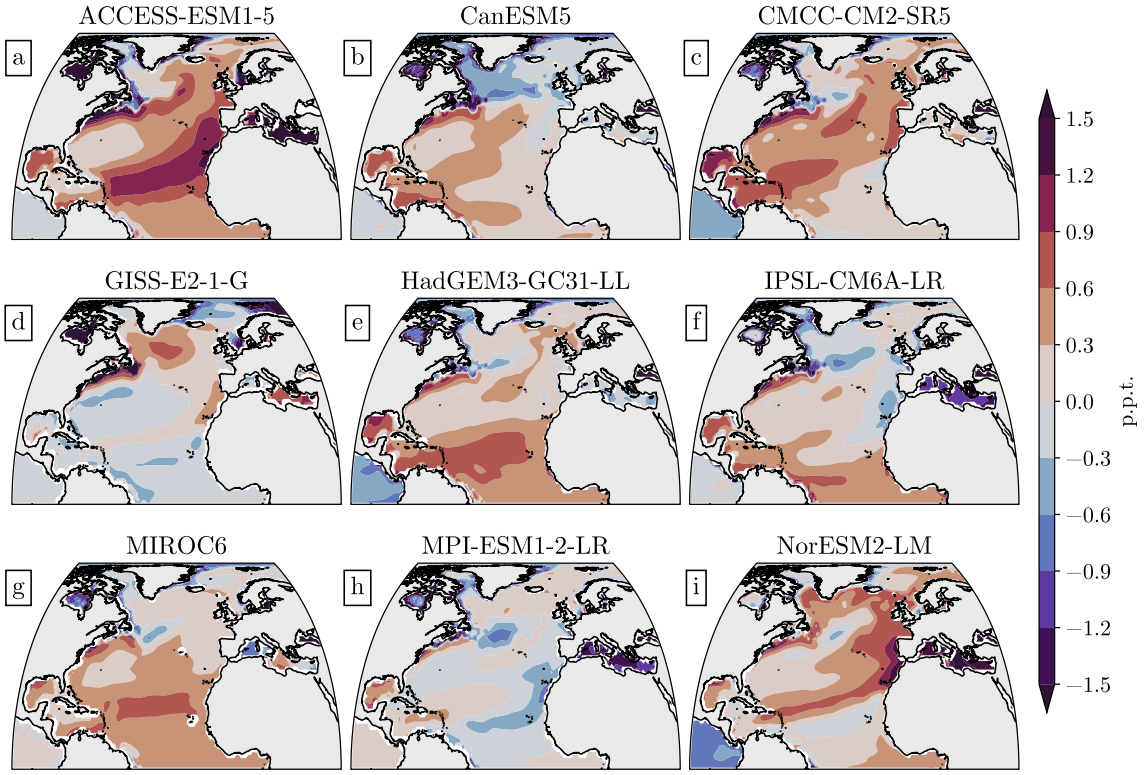


Fig. S14 Comparison between upper-ocean salinity climatology in models and observations. DJFM 1985–2014 upper-ocean salinity climatology difference between each model ensemble mean and the EN4 observations. Results do not change significantly for different time periods (not shown).

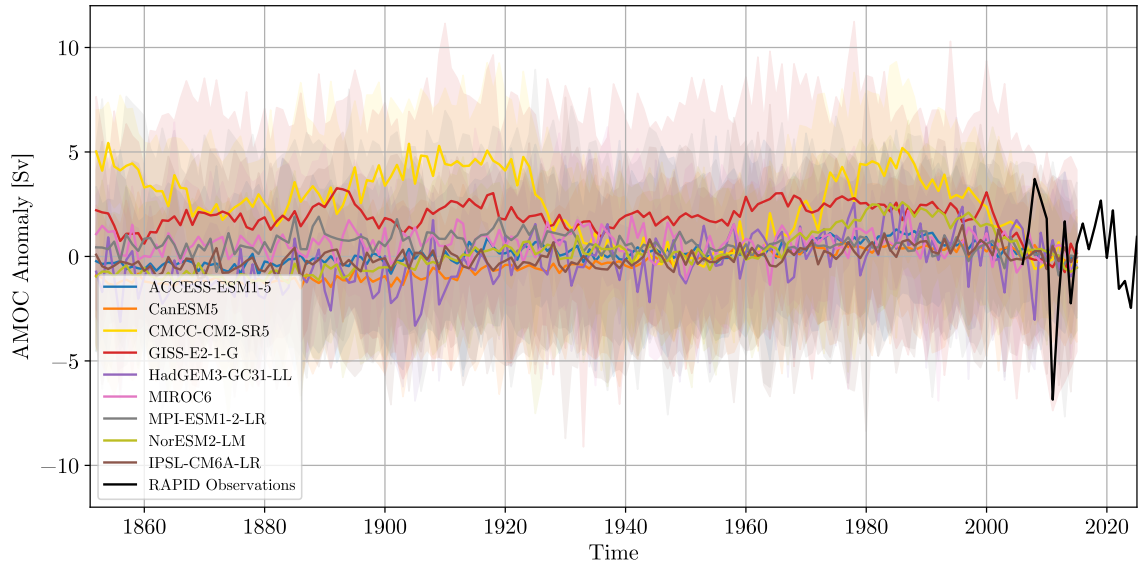


Fig. S15 Simulated and observed AMOC anomaly. DJFM AMOC anomaly for each of the used models (colored lines) and observed AMOC (black line, RAPID observations). For the models, solid lines represent ensemble means, while shades represent the max and min value across the ensemble for the respective model. The anomaly is computed using 2004–2014 as reference period. The AMOC index is defined as the maximum of the overturning streamfunction over depth at 26°N.